Artificially Creating Emergent Interfacial Antiferromagnetism and Its Manipulation in a Magnetic van der Waals Heterostructure

Xiangqi Wang,◆ Cong Wang,◆ Yupeng Wang,◆ Chunhui Ye, Azizur Rahman, Min Zhang, Suhan Son, Jun Tan,* Zengming Zhang,* Wei Ji,* Je-Geun Park, and Kai-Xuan Zhang*,◆

Read Online

ACCESS | Metrics & More | Article Recommendations | SI Supporting Information

ABSTRACT: van der Waals (vdW) magnets, with their two-dimensional (2D) atomic structures, provide a unique platform for exploring magnetism on the nanoscale. Although there have been numerous reports on their diverse quantum properties, the emergent interfacial magnetism—artificially created at the interface between two layered magnets—remains largely unexplored. This work presents observations of such emergent interfacial magnetism at the ferromagnet—antiferromagnet interface in a vdW heterostructure. We report the discovery of an intermediate Hall resistance plateau in the anomalous Hall loop indicative of emergent interfacial antiferromagnetism fostered by the heterointerface. This plateau can be stabilized and further manipulated under varying pressures but collapses at high pressures over 10 GPa. Our theoretical calculations reveal that charge transfer at the interface is pivotal in establishing the interlayer antiferromagnetic spin-exchange interaction. This work illuminates the previously unexplored emergent interfacial magnetism at a vdW interface comprising a ferromagnetic metal and an antiferromagnetic insulator and highlights its gradual evolution under increasing pressure. These findings enrich the portfolio of emergent interfacial magnetism and support further investigations of vdW magnetic interfaces and the development of next-generation spintronic devices.

KEYWORDS: artificially emergent interfacial antiferromagnetism, van-der-Waals heterostructure, ferromagnet/antiferromagnet heterostructure, intermediate Hall resistance plateau, advanced high-pressure nanotransport technique, interface charge transfer and magnetism
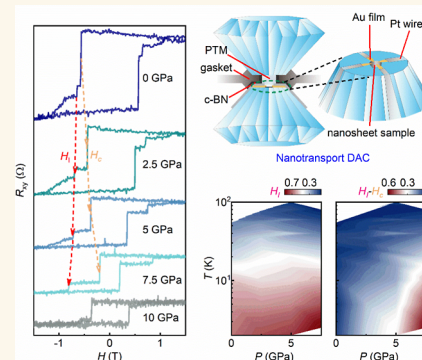
In recent years, magnetic van der Waals (vdW) materials[1−6] have emerged as a focal point of intense research, captivating the global scientific community. These layered magnetic materials provide a unique opportunity to investigate and realize a range of fundamental quantum phenomena in unprecedentedly true two-dimensional (2D) systems,[2,4,7−9] and introduce intriguing concepts in spintronics such as the gigantic spin filter effect[10−12] and intrinsic spin−orbit torque,[13−15] significantly advancing magnetic device applications.[10−24] Besides, vdW magnets naturally facilitate the assembly of multifunctional heterostructures, leveraging their vdW nature and unique magnetic features. Despite numerous studies on vdW magnetic heterostructures, the creation of emergent interfacial magnetism through proximity effects remains elusive. Furthermore, the manipulation of such emergent interfacial magnetism via external stimuli such as high pressure is even less explored and represents a frontier in this field.

Fe$_3$GeTe$_2$ (FGT)[25,26] represents the first studied vdW ferromagnetic metal of perpendicular magnetization with rich

intriguing properties.[13−15,27−33] Extensive research efforts have focused on tuning the magnetic properties of FGT through diverse methods,[26,34−40] but the creation of emergent magnetism by interfacing FGT with another vdW magnet is missing. To explore the possibility of emergent interfacial magnetism, we selected antiferromagnet MnPS$_3$ (MPS) to form a heterostructure with FGT (FGT/MPS) for two primary reasons: First, MPS is an insulating antiferromagnet,[41] which prevents the influence of free charge transport or magnetic stray fields, thereby isolating the interfacial effects. Second, as a representative Heisenberg model magnet,[1] MPS exhibits relatively isotropic exchange interactions along different
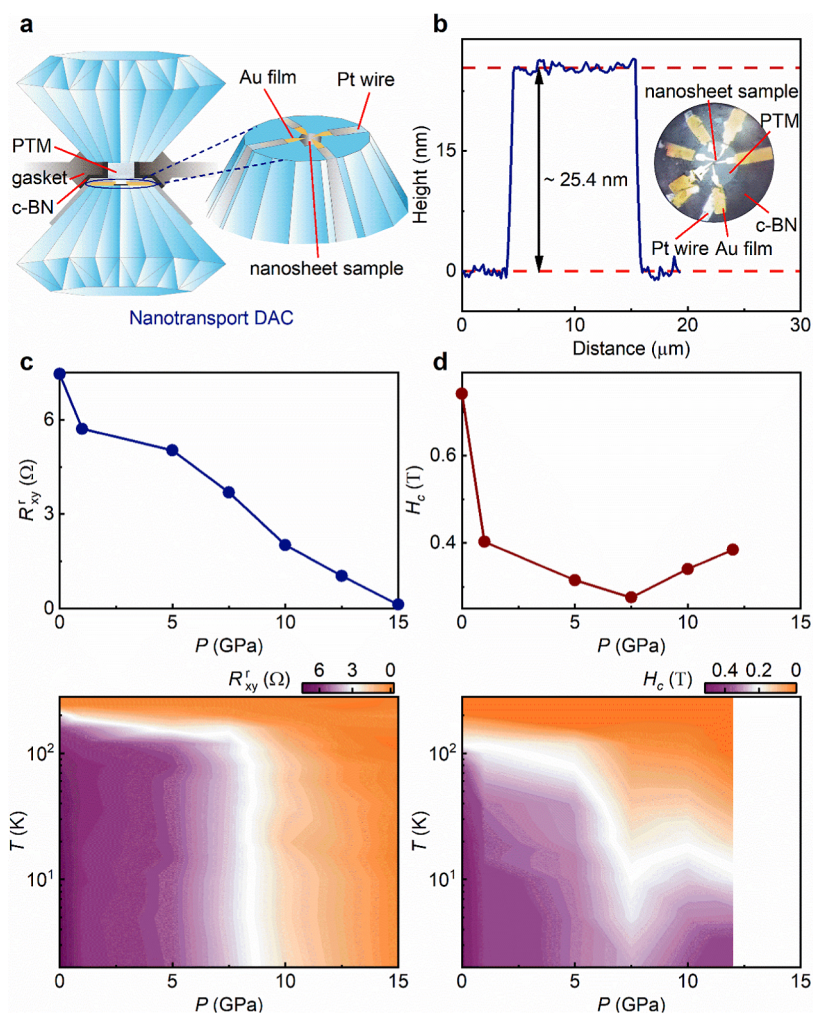
Figure 1. High-pressure modulation of nanotransport properties on a bare FGT nanoflake device. (a) 3D illustration of high-pressure nanotransport measurements. (b) Optical image of the bare FGT nanoflake device. The thickness was confirmed to be about 25.4 nm by atomic force microscopy. (c) Pressure-dependent remnant Hall resistance R_{xy}^r at 2 K. R_{xy}^r shows a gradually decreasing trend with increasing pressure, which is consistent with that of bulk FGT under pressure in our previous work.[36] The lower panel represents the temperature–pressure mapping of R_{xy}^r. (d) Pressure-dependent coercivity H_c at 2 K. H_c decreases below 10 GPa but increases above 10 GPa as the pressure increases. The lower panel represents the temperature–pressure mapping of H_c.

directions, which can accommodate any potentially required exchange interactions at the heterointerface. With the FGT/MPS heterostructure, we employed advanced high-pressure nanotransport techniques to manipulate and detect emergent interfacial magnetism. Distinct from the high-pressure studies on bulk vdW magnets, the high-pressure nanotransport of nanoscale thin-layers and atomic interface counterparts has rarely been reported, which is both conceptually and technically challenging.

Except for the above possible emergent interfacial magnetism, another significant contribution of our current work lies in elucidating the effect of interfacial charge transfer. In principle, interfacial charge transfer exists in a heterointerface generally and universally. However, the recognition and understanding of its modulation effect on the interfacial proximal interlayer magnetic coupling are rather lacking. Combined with theory, our experiments aim to demonstrate this modulation effect through the ferromagnet/antiferromagnet FGT/MPS heterostructure. Most importantly, this interfacial charge transfer and its modulation on interlayer magnetic coupling shall be a general principle applicable to all heterointerfaces beyond our

specific investigated case. This fundamental mechanism, although critical, has been largely overlooked, particularly in the field of 2D vdW magnets. It opens up exciting possibilities for manipulating magnetism and developing the corresponding quantum devices based on low-dimensional heterointerfaces.

In this work, we explore the interfacial effects within a vdW ferromagnetic/antiferromagnetic FGT/MPS heterostructure. We observe the development of an intermediate Hall resistance plateau during ferromagnetic switching induced by an external magnetic field in the heterostructure, which contrasts sharply with the abrupt switching observed in the bare FGT nanoflakes. This plateau indicates the formation of an emergent antiferromagnetic phase near the heterostructure interface, termed homointerlayer antiferromagnetism induced by the heterointerface. Furthermore, we find that the antiferromagnetic plateau region expands under high pressure, with the critical onset magnetic field required to disrupt the antiferromagnetic plateau increasing correspondingly. This stabilization of the emergent interfacial antiferromagnetic phase under pressure is likely due to the enhanced interfacial interactions as the high pressure brings the FGT and MPS
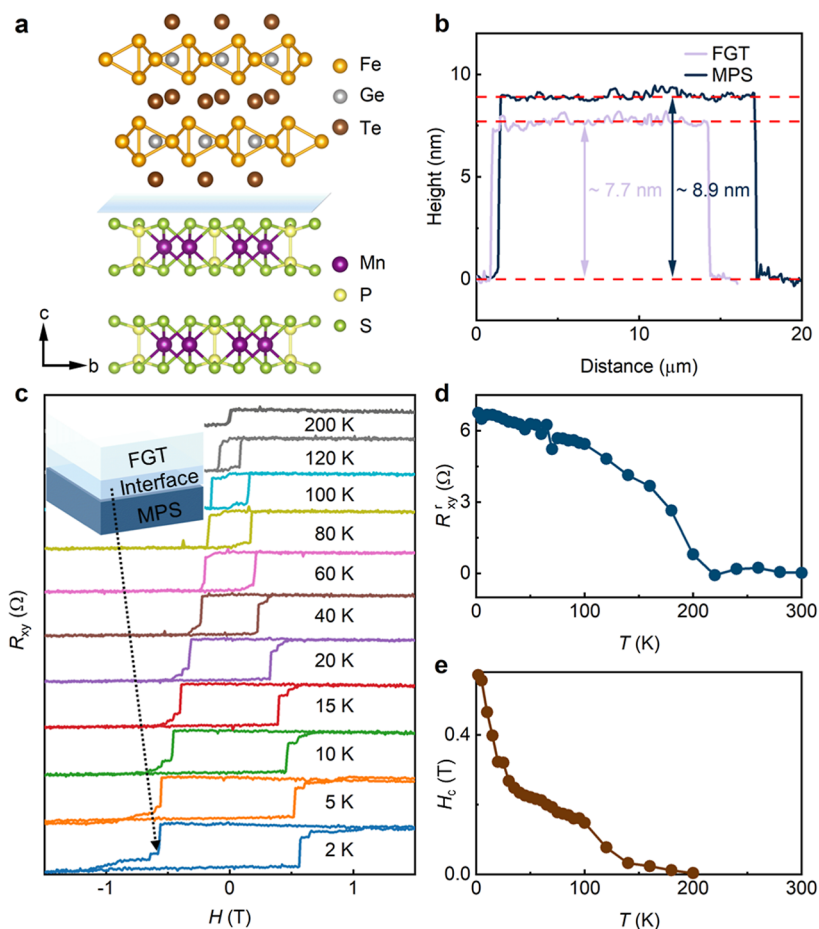
Figure 2. Emergent interfacial magnetism in the FGT/MPS heterostructure. (a) Illustration of the FGT/MPS heterostructure. (b) Thickness information on a typical real nanodevice with an FGT (7.7 nm)/MPS (8.9 nm) heterostructure. (c) $R_{xy}-H$ curves under zero pressure at various temperatures while sweeping the out-of-plane magnetic field H. The dashed black arrow highlights the intermediate Hall resistance plateau, which indicates emergent interfacial magnetism in the device. Such intermediate Hall resistance appears in both the positive and negative magnetic field directions symmetrically. The transport device's contribution is described by the three-layer toy model in the inset: the pristine FGT part and the interfacial magnetism part. (d,e) R_{xy}^{r} and H_c as a function of temperature T. They gradually decrease with increasing temperature, featuring a normal evolution of a typical ferromagnet FGT, except for the intermediate Hall plateau.

layers closer together. However, when the pressure exceeds 10 GPa, FGT undergoes a transition from a 2D to a 3D-like structure. Such a 2D-to-3D crossover can suppress the interfacial interactions between the MPS and the 3D-like FGT compared with the 2D FGT, resulting in a return to the single ferromagnetic switching behavior characteristic of the anomalous Hall effect without an intermediate plateau. Our theoretical calculations highlight the critical role of charge transfer at the interface in generating interfacial antiferromagnetic exchange interactions. These findings reveal the surprising emergence of interfacial antiferromagnetism and its comprehensive modulation under high pressure facilitated by our newly developed advanced high-pressure nanotransport technique. Our work not only elucidates the magnetic proximity effect and interfacial magnetism but also advances potential device applications in spintronics by utilizing the rapidly growing field of magnetic vdW materials.

RESULTS AND DISCUSSION

Effect of Pressure on a Bare FGT Nanoflake. As shown in Figure 1a, we developed a high-pressure nanotransport technique to measure the electrical transport properties of small-sized nanoflake devices under high pressure. Figure 1b

displays a typical optical image of the FGT nanoflake device with a thickness of approximately 25.4 nm, confirmed by atomic force microscopy. Figures S1 and S2 summarizes the transverse Hall resistance R_{xy} as a function of the applied out-of-plane magnetic field under various pressures. To understand the magnetic evolution under pressure, we extracted key magnetic parameters, namely, remnant Hall resistance R_{xy}^{r} and coercivity H_c at each temperature and pressure. As depicted in Figure 1c, R_{xy}^{r} decreases with increasing pressure until it vanishes at a fixed temperature (upper panel). Similarly, R_{xy}^{r} decreases with increasing temperature at a fixed pressure (lower panel), which is consistent with the typical temperature dependence of magnetization in ferromagnets.

Figure 1d illustrates the pressure and temperature dependence of coercivity H_c: both increasing pressure and temperature gradually suppress H_c. However, at extremely high pressures above 10 GPa, H_c starts to increase with pressure, indicating underlying changes, such as a 2D to 3D crossover under high pressure. There are at least two pieces of key evidence supporting such a 2D-to-3D crossover of FGT: First, previous Raman studies have shown a dynamical instability of the lattice[42] around 10 GPa, which can lead to structural transitions or a 2D to 3D-like crossover in structural,
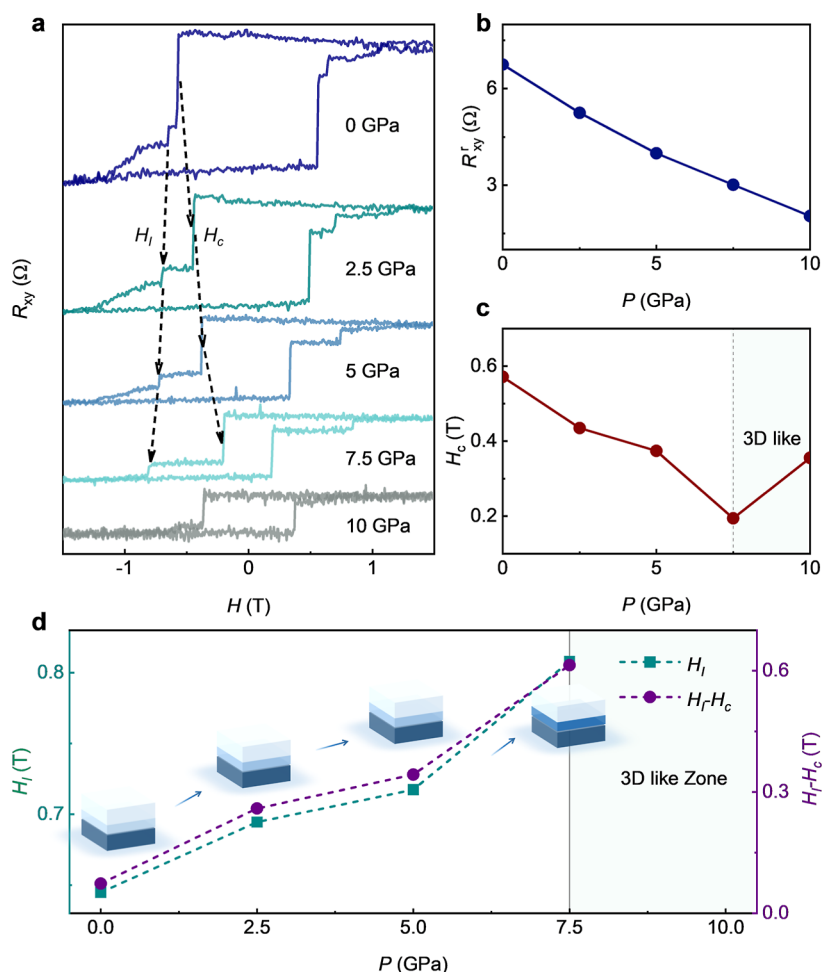
Figure 3. High-pressure tuning of the emergent interfacial magnetism. (a) $R_{xy}-H$ curves at 2 K under different pressures, e.g., 0, 2.5, 5, 7.5, and 10 GPa. The dashed black arrows highlight the pressure-dependent evolution of H_I and H_c, which represents the onset field for destruction of the interfacial magnetism and the coercivity of the FGT part. (b,c) R_{xy}^r and H_c of the pristine FGT part as a function of pressure in (a). They show a normal reduction trend, similar to that of the bare FGT nanoflakes in Figure 1 and the bulk FGT in our previous work.[36] (d) H_I and H_I-H_c as a function of applied pressure. Both H_I and H_I-H_c increase with increasing pressure, indicating enhanced stabilization of the emergent interfacial magnetism under high pressure. At the final extreme pressure, the intermediate plateau disappears, and the magnetic switching behaves uniformly and directly at 10 GPa. The magnetic evolution is also illustrated correspondingly with the inset schematic. The interfacial magnetism is represented by the light blue box, which becomes stronger as the pressure increases.

electronic, or magnetic properties frequently observed in highly pressurized vdW systems.[43−46] Second, our X-ray diffraction measurements of FGT reveal that the unit cell volume decreases with increasing pressure but shows a slower decreasing trend above 10 GPa with a noticeable kink (Figure S3).

The high-pressure nanotransport experiment on the FGT nanoflake provides more detailed information beyond high-pressure measurements on bulk FGT, such as the evolution of H_c, since the coercivity of bulk FGT is negligible. Nonetheless, the general pressure-induced magnetic evolution of bare FGT nanoflakes is similar to that of bulk FGT reported in our previous study,[36] validating our newly developed high-pressure nanotransport technique for nanodevices.

Emergent Interfacial Magnetism in the FGT/MPS Heterostructure. After examining the properties of bare FGT nanoflakes under high pressure, we now focus on the magnetic proximity effect in the FGT/MPS heterostructure. Figure 2a presents a schematic diagram of the crystal structure of the FGT/MPS heterostructure, and Figure 2b provides the thickness information on a real device, with FGT at 7.7 nm

and MPS at 8.9 nm. As MPS was intentionally selected due to its insulating properties and Heisenberg antiferromagnetism, the $R_{xy}-H$ curve of the heterostructure at zero pressure closely resembles that of pristine bare FGT nanoflakes at all temperatures (Figure 2c), primarily reflecting the transport behavior of the magnetic FGT. However, in stark contrast to the direct and smooth switching of bare FGT, the magnetic switching of the FGT/MPS heterostructure exhibits an intermediate Hall resistance plateau, as indicated by the dashed black arrow.

This emergent Hall plateau is a unique feature of the FGT/MPS hybrid system and is most prominent at low temperatures between 2 and 20 K, where both FGT and MPS maintain their ferromagnetic and antiferromagnetic ground states, respectively. This observation suggests the presence of distinct characteristics in the heterostructure, which can be attributed to the interfacial pinning effect, intrinsically originating from an emergent antiferromagnetism by the vdW heterointerface. This phenomenon is demonstrated in our case of a ferromagnetic-metal/antiferromagnetic−insulator interface. To illustrate this, we included a schematic inset showing three parts: FGT, the
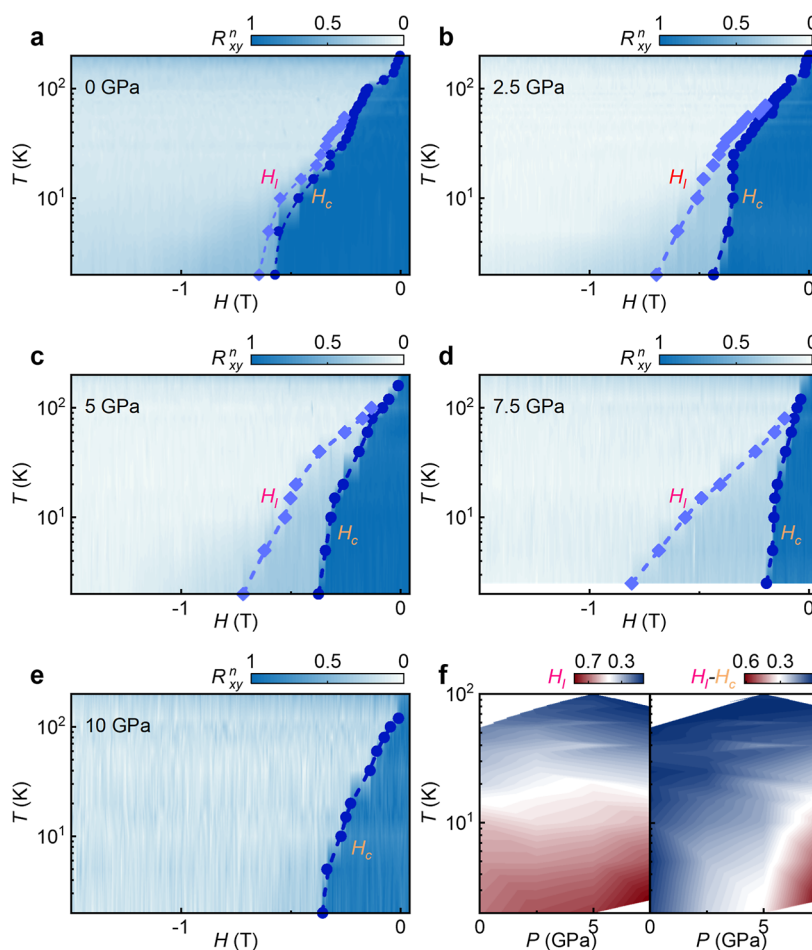
Figure 4. Temperature and pressure mapping of magnetism. (a−e) Temperature−magnetic field mapping of R_{xy}^{n} ($=R_{xy}/\max(R_{xy})$) for individual pressures, e.g., 0 (a), 2.5 (b), 5 (c), 7.5 (d), and 10 (e) GPa, respectively. H_{I} and H_{c} are highlighted correspondingly. (f) Temperature−pressure mapping of H_{I} and $H_{I}−H_{c}$, derived from (a−e). Note that both H_{I} and $H_{I}−H_{c}$ increase at lower temperatures and higher pressures, as does the interfacial magnetism, which is mostly strengthened at the right-bottom corner with the reddest color.

interface, and the insulating MPS, to describe the transport contributions from both the FGT and the interfacial region within the entire device. Apart from this difference, all other features, such as the temperature-dependent variations in R_{xy}^{r} and H_c, are similar to the typical ferromagnetic behavior of pristine FGT (Figure 2d,e).

Pressure Modulation of Emergent Interfacial Magnetism. To better understand emergent interfacial magnetism, we performed high-pressure nanotransport measurements on the FGT/MPS heterostructure. Figure 3a presents the $R_{xy}−H$ curves of the FGT/MPS heterostructure at 2 K under various pressures. The dashed black lines highlight H_c and H_I, representing the coercivity of the FGT component and the critical onset magnetic field required to disrupt the interfacial magnetism, respectively. As shown in Figure 3b,c, R_{xy}^{r} decreases with increasing pressure, and H_c decreases below 10 GPa but increases above 10 GPa, which is consistent with the behavior observed in bare FGT nanoflakes (Figure 1) and bulk FGT in our previous study,[36] reflecting the intrinsic properties of pristine FGT. In sharp contrast, H_I and $H_I−H_c$ increase with increasing pressure (Figure 3d), which cannot be attributed to the FGT component but rather to the emergent interfacial magnetism. This finding indicates that the interfacial magnetism is further stabilized by increasing pressure, which contrasts with the pressure-weakened ferromagnetism of FGT

and suggests the antiferromagnetic nature of the interfacial magnetism. Applying higher pressure brings MPS into a greater proximity to FGT, thereby enhancing the interfacial interaction. This increased interfacial interaction aligns with the pressure-stabilized intermediate Hall plateau, further corroborating that the plateau originates from emergent interfacial antiferromagnetism within the heterostructure.

It is noteworthy that MPS well preserves its insulating and antiferromagnetic characteristics below 10 GPa.[47−49] However, at approximately 10 GPa, FGT undergoes a 2D to 3D-like crossover, which significantly suppresses the interfacial interaction between MPS and 3D-FGT. Consequently, the magnetic switching becomes uniform, without interfacial contributions (Figure 3, parts a and d). On the basis of these analyses, we constructed a schematic of the magnetism evolution in the heterostructure under pressure, as shown in the inset of Figure 3d. As the pressure increases, the ferromagnetism of the FGT component (indicated in white) gradually weakens, whereas emergent interfacial antiferromagnetism at the FGT/MPS interface (indicated in light blue) increasingly stabilizes. At extreme pressure, the interfacial effect vanishes due to the 2D to 3D-like crossover of FGT, resulting in uniform and direct magnetic switching.

Temperature and Pressure Mapping of the Interfacial Magnetism. To provide a comprehensive overview of the
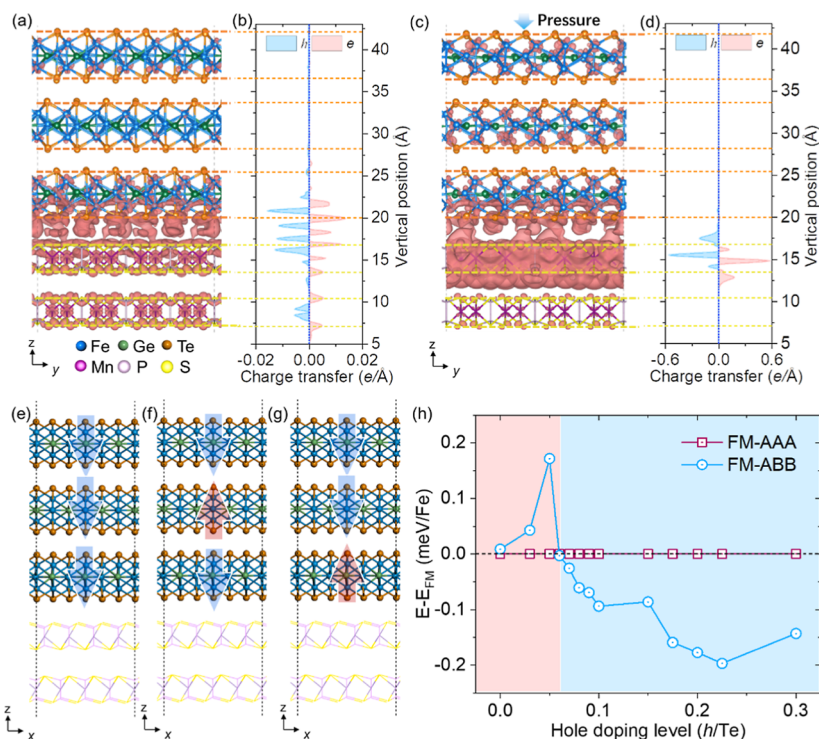
Figure 5. Substrate and pressure-modulated magnetism of few-layer FGT. (a−d) Heterointerlayer differential charge density (a,c) and corresponding line profiles along z (b,d) of the FGT trilayer stacked on the MPS bilayer without (a,b) and with (c,d) vertical strain. An isosurface value of 0.001 e Bohr^{-3} was used. The red isosurface contours represent charge accumulation after layer stacking. The blue, green, brown, purple, pink, and yellow balls represent the Fe atoms, Ge atoms, Te atoms, Mn atoms, P atoms, and S atoms, respectively. (e−g) Schematic representations of interlayer magnetic orders, including FM-AAA (e), FM-ABA (f), and FM-ABB (g) are depicted. The yellow and purple lines correspond to the MPS substrate for clarity. The blue and red arrows represent two antiparallel orientations of magnetic moments on Fe atoms. (h) Relative total energies of the FM-AAA (red rectangles) and FM-AAB (blue circles) orders of the FGT trilayer as a function of local hole doping on bottom Te atoms. The FM-AAA order was chosen as the reference zero.

evolution of interfacial magnetism, we performed high-pressure measurements of the $R_{xy}-H$ curves across various temperatures. Figure 4a−e displays the temperature−magnetic field maps of the normalized Hall resistance $R_{xy}{}^n$ at 0, 2.5, 5, 7.5, and 10 GPa, respectively. Here, $R_{xy}{}^n$ is defined as $R_{xy}/\max(R_{xy})$ at different magnetic fields H. In these mappings, H_c and H_I are highlighted and increase as the system temperature decreases. However, H_I increases much more rapidly than H_c does with decreasing temperature, particularly at higher pressures. Notably, H_c shows a suppressed rate of increase with decreasing temperature as the pressure increases, whereas H_I evolves in the opposite direction. This results in a larger discrepancy between H_I and H_c, i.e., H_I-H_c increases under higher pressures. This pressure-dependent behavior is similar to the results observed at the lowest temperature of 2 K in Figure 3. At a high pressure of 10 GPa, the interfacial magnetism disappears and the H_c of the uniform magnetic switching starts to increase compared with that at 7.5 GPa, which is also consistent with the pressure-dependent evolution at 2 K shown in Figure 3. More importantly, we plotted the temperature−pressure maps of H_I and H_I-H_c in Figure 4f by extracting data from Figure 4a−e. As shown, both H_I and H_I-H_c increase as the temperature decreases or the pressure increases. In other words, the interfacial magnetism can be modulated by both temperature and pressure and is most pronounced in the low-temperature−high-pressure regime, as indicated by the reddest region in the bottom-right corner of the map.

Theoretical Calculations. Density functional theory calculations were performed to elucidate the substrate-modulated magnetism in few-layer FGT. A 3×33L-FGT/2×2BL-MPS supercell (Figure S7) was constructed to model the experimentally obtained FGT/MPS heterostructure, which corresponds to substrate-induced compressive in-plane strains of 2.1% (1.7%) along the x-axis (y-axis) and lowest total energy within a fairly large search space. Our calculations reveal that while the substrate-induced interfacial strain weakens the interlayer ferromagnetic coupling of FGT, it does not render the antiferromagnetic state as the ground state (Table S1). Figure 5a,b illustrates charge accumulation upon stacking FGT on an MPS, indicating that charge transfer predominantly occurs between these interfacial layers of the heterostructure. Given the valence band edge at −6.2 eV relative to the vacuum level for MPS and a work function of 5.0 eV for FGT, electrons transfer from FGT to MPS in the FGT/MPS heterostructure, resulting in local hole doping to the interfacial FGT layer and thereby modifying the interfacial magnetic couplings.

In the freestanding trilayer FGT, the most energetically stable configuration features both intra- and interlayer ferromagnetic orders (Figure 5e) compared to other magnetic configurations (Figure 5f,g) by at least 0.39 meV/Fe (Table S1). The local hole doping induced by the MPS substrate weakens the ferromagnetic interlayer coupling between adjacent FGT layers.[26] Consequently, intralayer ferromagnetic and interlayer ferrimagnetic orders (FM-AAB, Figure 5g) become energetically favorable over the pure ferromagnetic order (Table S1). The interfacial interlayer antiferromagnetic

coupling causes the interfacial and bulk FGT layers to respond differently under an external field, potentially leading to the Hall resistance plateau observed in our experiments (Figure 2).

To validate this mechanism, we introduced local hole doping into the lowest Te layer of the freestanding trilayer FGT to model the interfacial charge transfer. Our results show that the FM-AAB configuration becomes the magnetic ground state when the hole doping concentration exceeds 0.05 h/Te (Figure 5h). Moreover, as the doping concentration increases from 0.05 to 0.225 h/Te, the relative stability of the FM-AAB state is further enhanced. The reduction in the interfacial distance between FGT and MPS under external pressure increases the hole doping concentration (Figure 5c,d), likely contributing to the observed enhancement of the coercive field H_I under moderate pressure ranging from 2.5 to 7.5 GPa in our experiments. At 10 GPa, FGT, most likely, undergoes a transition from a 2D to a 3D-like structure,[42] leading to a significant suppression of interfacial AFM magnetic coupling and causing the interface to become ferromagnetic as the ground state (Table S1), consistent with experimentally observed disappearance of the Hall resistance plateau.

CONCLUSIONS

In summary, we artificially induced emergent interfacial magnetism at the vdW magnetic interface in the FGT/MPS heterostructure. This emergent interfacial magnetism manifests as an intermediate Hall resistance plateau within the anomalous Hall effect and exhibits a markedly different evolutionary trend compared to ferromagnetic FGT under high pressures. Our theoretical analysis suggests that interfacial charge transfer may be responsible for the emergence and reinforcement of interfacial antiferromagnetism. Our work provides a valuable example of emergent interfacial magnetism and its manipulation, offering insights into interface magnetism engineering, 2D magnetic materials, and the development of advanced spintronic devices.

METHODS

Preparation of FGT, MPS Single Crystals, Nanoflake Devices, and FGT/MPS Heterostructures. High-quality FGT single crystals were grown via the chemical vapor transport technique.[35,39] A stoichiometric amount of Fe, Ge, and Te powder (Fe purity, 99.9%; Ge purity, 99.999%; Te purity, 99.999%) with a molar ratio of 3:1:2 was mixed and sealed in an evacuated quartz tube. Iodine was employed as a transport agent. The quartz tube was heated with a temperature gradient of 1023/973 K for several days. Thin flake crystals of millimeter size with metallic luster were obtained after natural cooling to room temperature. The crystals were kept in vacuum-sealed tubes to prevent possible oxidation.

MPS single crystals were also prepared via the chemical vapor transport method. A stoichiometric mixture of high-purity Mn, P, and S powders with a molar ratio of 1:1:3 was mixed and sealed in an evacuated quartz tube with iodine as a transport agent. The quartz tube was also heated with a temperature gradient of 1023−973 K for several days. Plate-like MPS single crystals were obtained after natural cooling to room temperature.

Few-layer FGT and MPS samples were obtained by exfoliating bulk samples onto the PDMS substrates. The heterostructures for transport measurements were fabricated by sequentially transferring FGT and MPS onto the diamond surface with prepatterned electrodes.

High-Pressure Nanotransport Measurements. Nonmagnetic beryllium copper (BeCu) diamond anvil cells with 500 μm culet type-2 diamonds were used for high-pressure experiments. Platinum (Pt) electrodes were positioned on a tungsten gasket, which was coated with a mixture of cubic boron nitride (c-BN) and epoxy for the insulation. Daphne 7373 was employed as the pressure-transmitting medium, and the pressure was calibrated by using ruby fluorescence.

After the Pt electrodes on the gasket were prepared, their relative positions with respect to the diamond anvil were carefully recorded. Titanium/gold (Ti/Au, 5/100 nm) electrodes were then patterned on the diamond surface by using photolithography and deposited at the corresponding locations. This ensured reliable electrical connections between the FGT/MPS sample, placed onto the diamond and the Pt electrodes.

For transport measurements, the Physical Property Measurement System (PPMS) was utilized, employing standard low-frequency lock-in amplifier techniques with an excitation current of 100 nA. This setup allowed for precise electrical characterization of the sample under high-pressure conditions.

COMPUTATIONAL METHODS

The calculations were performed via the generalized gradient approximation and projector augmented-wave method[50] as implemented in the Vienna ab initio calculation package.[51] Dispersion correction was considered in Grimme's semiempirical D3 scheme[52] in combination with the PBE functional (PBE-D3). This combination achieves an accuracy comparable to that of the optB86b-vdW functional for describing the geometric properties of layered materials at a lower computational cost.[53] On-site Coulomb interactions on Fe and Mn 3d orbitals are characterized via U and J values, namely, U = 3.6 eV and J = 0.2 eV for Fe^{3+}, U = 4.6 eV, and J = 1.0 eV for Fe^{2+} and U = 4.0 eV and J = 0 eV for Mn^{2+}, as revealed via a linear response method[37,54,55] via the PlusU package. A uniform Monkhorst−Pack k-mesh of size 15 × 15 × 3 was adopted for integration over the Brillouin zone of an FGT bulk unit cell. The shape and volume of the unit cell of pristine FGT were fully optimized, and all the atoms were allowed to relax until the residual force per atom was less than 0.01 eV/Å. A 3 × 3trilayer FGT/2 × 2bilayer MPS magnetic supercell was adopted for the calculations of structure optimization and magnetic ground state (Figure 5) to include the substrate effect, in which an MP k-mesh of 3 × 1 × 1 was used. A kinetic energy cutoff of 400 eV for the plane-wave basis set was used for both structural relaxation and electronic structure calculations of FGT on MPS heterostructure models. A sufficiently large vacuum layer of over 20 Å along the out-of-plane direction was adopted to eliminate the interaction among layers. Charge doping on Te atoms was realized with the ionic potential method.[56,57] For hole doping, electrons were removed from the valence band by adding a negative potential into the 4d core level of Te. This method ensured that the doped charges were located around the Te atoms. It also retained the neutrality of the whole supercell without introducing a background charge, which eliminated the effects of compensating charges.

ASSOCIATED CONTENT

ⓈI Supporting Information

The Supporting Information is available free of charge at https://pubs.acs.org/doi/10.1021/acsnano.4c16450.

> Discussions on the interfacial magnetism of the FGT/MPS heterostructure; anomalous Hall measurement of bare FGT under 0 GPa; R_{xy}−H curves of the FGT nanoflake device at different temperatures under various pressures; lattice constants and unit cell volume of FGT as a function of pressure; R_{xx}−T of FGT under diverse pressures; R_{xy}−H curves of the FGT/MPS heterostructure at different temperatures under various pressures.; T−P mapping of H_c in the FGT/MPS heterostructure; top and side views of the heterostructure model; certain exchange bias effect in the samples; and relative total energies of the freestanding and substrate-supported 3L FGT (PDF)

AUTHOR INFORMATION

Corresponding Authors

Jun Tan − *Testing Center, Jihua Laboratory, Foshan 528000, China*; Email: tanjun@jihualab.ac.cn

Zengming Zhang − *Deep Space Exploration Laboratory, The Centre for Physical Experiments and CAS Key Laboratory of Strongly Coupled Quantum Matter Physics, Department of Physics, School of Physical Sciences, University of Science and Technology of China, Hefei 230026, China*; ⓞ orcid.org/0000-0001-8245-9955; Email: zzm@ustc.edu.cn

Wei Ji − *Beijing Key Laboratory of Optoelectronic Functional Materials & Micro-Nano Devices, School of Physics, Renmin University of China, Beijing 100872, China; Key Laboratory of Quantum State Construction and Manipulation (Ministry of Education), Renmin University of China, Beijing 100872, China*; ⓞ orcid.org/0000-0001-5249-6624; Email: wji@ruc.edu.cn

Kai-Xuan Zhang − *Department of Physics and Astronomy, Seoul National University, Seoul 08826, South Korea; Center for Quantum Materials, Department of Physics and Astronomy and Institute of Applied Physics, Seoul National University, Seoul 08826, South Korea*; ⓞ orcid.org/0000-0002-9958-6018; Email: kxzhang.research@gmail.com

Authors

Xiangqi Wang − *Testing Center, Jihua Laboratory, Foshan 528000, China*

Cong Wang − *Beijing Key Laboratory of Optoelectronic Functional Materials & Micro-Nano Devices, School of Physics, Renmin University of China, Beijing 100872, China; Key Laboratory of Quantum State Construction and Manipulation (Ministry of Education), Renmin University of China, Beijing 100872, China*

Yupeng Wang − *Deep Space Exploration Laboratory, The Centre for Physical Experiments and CAS Key Laboratory of Strongly Coupled Quantum Matter Physics, Department of Physics, School of Physical Sciences, University of Science and Technology of China, Hefei 230026, China*

Chunhui Ye − *Deep Space Exploration Laboratory, The Centre for Physical Experiments and CAS Key Laboratory of Strongly Coupled Quantum Matter Physics, Department of Physics, School of Physical Sciences, University of Science and Technology of China, Hefei 230026, China*

Azizur Rahman − *Deep Space Exploration Laboratory, The Centre for Physical Experiments and CAS Key Laboratory of Strongly Coupled Quantum Matter Physics, Department of Physics, School of Physical Sciences, University of Science and Technology of China, Hefei 230026, China*

Min Zhang − *Institutes of Physical Science and Information Technology, Anhui University, Hefei 230601, China*

Suhan Son − *Department of Physics and Astronomy, Seoul National University, Seoul 08826, South Korea; Center for Quantum Materials, Department of Physics and Astronomy and Institute of Applied Physics, Seoul National University, Seoul 08826, South Korea; Present Address: Department of Physics, University of Michigan, Ann Arbor, MI 48109, USA*

Je-Geun Park − *Department of Physics and Astronomy, Seoul National University, Seoul 08826, South Korea; Center for Quantum Materials, Department of Physics and Astronomy and Institute of Applied Physics, Seoul National University, Seoul 08826, South Korea*; ⓞ orcid.org/0000-0002-3930-4226

Complete contact information is available at:
https://pubs.acs.org/10.1021/acsnano.4c16450

Author Contributions

♦X.W., C.W., Y.W., and K.-X.Z. contributed equally to this work.

Notes

The authors declare no competing financial interest.

REFERENCES

(1) Park, J. G. Opportunities and challenges of 2D magnetic van der Waals materials: magnetic graphene? *J. Phys.: Condens. Matter* **2016**, *28*, 301001.

(2) Lee, J. U.; Lee, S.; Ryoo, J. H.; Kang, S.; Kim, T. Y.; Kim, P.; Park, C. H.; Park, J. G.; Cheong, H. Ising-Type Magnetic Ordering in Atomically Thin FePS₃. *Nano Lett.* **2016**, *16*, 7433−7438.

(3) Huang, B.; Clark, G.; Navarro-Moratalla, E.; Klein, D. R.; Cheng, R.; Seyler, K. L.; Zhong, D.; Schmidgall, E.; McGuire, M. A.; Cobden, D. H.; Yao, W.; Xiao, D.; Jarillo-Herrero, P.; Xu, X. Layer-dependent ferromagnetism in a van der Waals crystal down to the monolayer limit. *Nature* **2017**, *546*, 270−273.

(4) Gong, C.; Li, L.; Li, Z.; Ji, H.; Stern, A.; Xia, Y.; Cao, T.; Bao, W.; Wang, C.; Wang, Y.; Qiu, Z. Q.; Cava, R. J.; Louie, S. G.; Xia, J.; Zhang, X. Discovery of intrinsic ferromagnetism in two-dimensional van der Waals crystals. *Nature* **2017**, *546*, 265−269.

(5) Burch, K. S.; Mandrus, D.; Park, J. G. Magnetism in two-dimensional van der Waals materials. *Nature* **2018**, *563*, 47−52.

(6) Zhang, K.-X.; Park, G.; Lee, Y.; Kim, B. H.; Park, J.-G. Magnetoelectric effect in van der Waals magnets. *npj Quantum Mater.* **2025**, *10*, 6.

(7) Mermin, N. D.; Wagner, H. Absence of ferromagnetism or antiferromagnetism in one-or two-dimensional isotropic Heisenberg models. *Phys. Rev. Lett.* **1966**, *17*, 1133−1136.

(8) Yang, B.; Goh, Y. M.; Sung, S. H.; Ye, G.; Biswas, S.; Kaib, D. A. S.; Dhakal, R.; Yan, S.; Li, C.; Jiang, S.; Chen, F.; Lei, H.; He, R.; Valenti, R.; Winter, S. M.; Hovden, R.; Tsen, A. W. Magnetic

anisotropy reversal driven by structural symmetry-breaking in monolayer alpha-RuCl₃. *Nat. Mater.* **2023**, *22*, 50−57.

(9) Kim, K.; Lim, S. Y.; Lee, J. U.; Lee, S.; Kim, T. Y.; Park, K.; Jeon, G. S.; Park, C. H.; Park, J. G.; Cheong, H. Suppression of magnetic ordering in XXZ-type antiferromagnetic monolayer NiPS₃. *Nat. Commun.* **2019**, *10*, 345.

(10) Song, T.; Cai, X.; Tu, M. W.; Zhang, X.; Huang, B.; Wilson, N. P.; Seyler, K. L.; Zhu, L.; Taniguchi, T.; Watanabe, K.; McGuire, M. A.; Cobden, D. H.; Xiao, D.; Yao, W.; Xu, X. Giant tunneling magnetoresistance in spin-filter van der Waals heterostructures. *Science* **2018**, *360*, 1214−1218.

(11) Klein, D. R.; MacNeill, D.; Lado, J. L.; Soriano, D.; Navarro-Moratalla, E.; Watanabe, K.; Taniguchi, T.; Manni, S.; Canfield, P.; Fernandez-Rossier, J.; Jarillo-Herrero, P. Probing magnetism in 2D van der Waals crystalline insulators via electron tunneling. *Science* **2018**, *360*, 1218−1222.

(12) Wang, Z.; Gutierrez-Lezama, I.; Ubrig, N.; Kroner, M.; Gibertini, M.; Taniguchi, T.; Watanabe, K.; Imamoglu, A.; Giannini, E.; Morpurgo, A. F. Very large tunneling magnetoresistance in layered magnetic semiconductor CrI₃. *Nat. Commun.* **2018**, *9*, 2516.

(13) Zhang, K.; Han, S.; Lee, Y.; Coak, M. J.; Kim, J.; Hwang, I.; Son, S.; Shin, J.; Lim, M.; Jo, D.; Kim, K.; Kim, D.; Lee, H.-W.; Park, J.-G. Gigantic current control of coercive field and magnetic memory based on nm-thin ferromagnetic van der Waals Fe₃GeTe₂. *Adv. Mater.* **2021**, *33*, 2004110.

(14) Johansen, Ø.; Risinggård, V.; Sudbø, A.; Linder, J.; Brataas, A. Current Control of Magnetism in Two-Dimensional Fe₃GeTe₂. *Phys. Rev. Lett.* **2019**, *122*, 217203.

(15) Zhang, K.-X.; Ju, H.; Kim, H.; Cui, J.; Keum, J.; Park, J.-G.; Lee, J. S. Broken inversion symmetry in van der Waals topological ferromagnetic metal iron germanium telluride. *Adv. Mater.* **2024**, *36*, 2312824.

(16) Wang, Z.; Sapkota, D.; Taniguchi, T.; Watanabe, K.; Mandrus, D.; Morpurgo, A. F. Tunneling Spin Valves Based on Fe₃GeTe₂/hBN/Fe₃GeTe₂ van der Waals Heterostructures. *Nano Lett.* **2018**, *18*, 4303−4308.

(17) Zhu, W.; Lin, H.; Yan, F.; Hu, C.; Wang, Z.; Zhao, L.; Deng, Y.; Kudrynskyi, Z. R.; Zhou, T.; Kovalyuk, Z. D.; Zheng, Y.; Patane, A.; Zutic, I.; Li, S.; Zheng, H.; Wang, K. Large Tunneling Magneto-resistance in van der Waals Ferromagnet/Semiconductor Hetero-junctions. *Adv. Mater.* **2021**, *33*, 2104658.

(18) Min, K. H.; Lee, D. H.; Choi, S. J.; Lee, I. H.; Seo, J.; Kim, D. W.; Ko, K. T.; Watanabe, K.; Taniguchi, T.; Ha, D. H.; Kim, C.; Shim, J. H.; Eom, J.; Kim, J. S.; Jung, S. Tunable spin injection and detection across a van der Waals interface. *Nat. Mater.* **2022**, *21*, 1144−1149.

(19) Zhu, W.; Zhu, Y.; Zhou, T.; Zhang, X.; Lin, H.; Cui, Q.; Yan, F.; Wang, Z.; Deng, Y.; Yang, H.; Zhao, L.; Zutic, I.; Belashchenko, K. D.; Wang, K. Large and tunable magnetoresistance in van der Waals ferromagnet/semiconductor junctions. *Nat. Commun.* **2023**, *14*, 5371.

(20) Wang, X.; Tang, J.; Xia, X.; He, C.; Zhang, J.; Liu, Y.; Wan, C.; Fang, C.; Guo, C.; Yang, W.; Guang, Y.; Zhang, X.; Xu, H.; Wei, J.; Liao, M.; Lu, X.; Feng, J.; Li, X.; Peng, Y.; Wei, H.; Yang, R.; Shi, D.; Zhang, X.; Han, Z.; Zhang, Z.; Zhang, G.; Yu, G.; Han, X. Current-driven magnetization switching in a van der Waals ferromagnet Fe₃GeTe₂. *Sci. Adv.* **2019**, *5*, No. eaaw8904.

(21) Zhang, K.; Lee, Y.; Coak, M. J.; Kim, J.; Son, S.; Hwang, I.; Ko, D. S.; Oh, Y.; Jeon, I.; Kim, D.; Zeng, C.; Lee, H.-W.; Park, J.-G. Highly efficient nonvolatile magnetization switching and multi-level states by current in single van der Waals topological ferromagnet Fe₃GeTe₂. *Adv. Funct. Mater.* **2021**, *31*, 2105992.

(22) Zhang, K.-X.; Xu, H.; Keum, J.; Wang, X.; Liu, M.; Chen, Z. Unexpected versatile electrical transport behaviors of ferromagnetic nickel films. *J. Phys.: Condens. Matter* **2024**, *36*, 235801.

(23) Cui, J.; Zhang, K.-X.; Park, J.-G. All van der Waals Three-Terminal SOT-MRAM Realized by Topological Ferromagnet Fe₃GeTe₂. *Adv. Electron. Mater.* **2024**, *10*, 2400041.

(24) Keum, J.; Zhang, K.-X.; Cheon, S.; Kim, H.; Cui, J.; Park, G.; Chang, Y.; Kim, M.; Lee, H.-W.; Park, J.-G. Novel magnetic-field-free

(25) Tan, C.; Lee, J.; Jung, S. G.; Park, T.; Albarakati, S.; Partridge, J.; Field, M. R.; McCulloch, D. G.; Wang, L.; Lee, C. Hard magnetic properties in nanoflake van der Waals Fe₃GeTe₂. *Nat. Commun.* **2018**, *9*, 1554.

(26) Deng, Y.; Yu, Y.; Song, Y.; Zhang, J.; Wang, N. Z.; Sun, Z.; Yi, Y.; Wu, Y. Z.; Wu, S.; Zhu, J.; Wang, J.; Chen, X. H.; Zhang, Y. Gate-tunable room-temperature ferromagnetism in two-dimensional Fe₃GeTe₂. *Nature* **2018**, *563*, 94−99.

(27) Martin, F.; Lee, K.; Schmitt, M.; Liedtke, A.; Shahee, A.; Simensen, H. T.; Scholz, T.; Saunderson, T. G.; Go, D.; Gradhand, M.; Mokrousov, Y.; Denneulin, T.; Kovács, A.; Lotsch, B.; Brataas, A.; Kläui, M. Strong bulk spin-orbit torques quantified in the van der Waals ferromagnet Fe₃GeTe₂. *Mater. Res. Lett.* **2023**, *11*, 84−89.

(28) Robertson, I. O.; Tan, C.; Scholten, S. C.; Healey, A. J.; Abrahams, G. J.; Zheng, G.; Manchon, A.; Wang, L.; Tetienne, J.-P. Imaging current control of magnetization in Fe₃GeTe₂ with a widefield nitrogen-vacancy microscope. *2D Mater.* **2023**, *10*, 015023.

(29) Zhang, G.; Wu, H.; Yang, L.; Jin, W.; Xiao, B.; Zhang, W.; Chang, H. Room-temperature Highly-Tunable Coercivity and Highly-Efficient Multi-States Magnetization Switching by Small Current in Single 2D Ferromagnet Fe₃GaTe₂. *ACS Mater. Lett.* **2024**, *6*, 482−488.

(30) Yan, S.; Tian, S.; Fu, Y.; Meng, F.; Li, Z.; Lei, H.; Wang, S.; Zhang, X. Highly Efficient Room-Temperature Nonvolatile Magnetic Switching by Current in Fe₃GaTe₂ Thin Flakes. *Small* **2024**, *20*, 2311430.

(31) Deng, Y.; Wang, M.; Xiang, Z.; Zhu, K.; Hu, T.; Lu, L.; Wang, Y.; Ma, Y.; Lei, B.; Chen, X. Room-Temperature Highly Efficient Nonvolatile Magnetization Switching by Current in van der Waals Fe₃GaTe₂ Devices. *Nano Lett.* **2024**, *24*, 9302−9310.

(32) Kim, K.; Seo, J.; Lee, E.; Ko, K. T.; Kim, B. S.; Jang, B. G.; Ok, J. M.; Lee, J.; Jo, Y. J.; Kang, W.; Shim, J. H.; Kim, C.; Yeom, H. W.; Il Min, B.; Yang, B. J.; Kim, J. S. Large anomalous Hall current induced by topological nodal lines in a ferromagnetic van der Waals semimetal. *Nat. Mater.* **2018**, *17*, 794−799.

(33) Xu, J.; Phelan, W. A.; Chien, C. L. Large Anomalous Nernst Effect in a van der Waals Ferromagnet Fe₃GeTe₂. *Nano Lett.* **2019**, *19*, 8250−8254.

(34) Zheng, G.; Xie, W.-Q.; Albarakati, S.; Algarni, M.; Tan, C.; Wang, Y.; Peng, J.; Partridge, J.; Farrar, L.; Yi, J.; Xiong, Y.; Tian, M.; Zhao, Y.-J.; Wang, L. Gate-Tuned Interlayer Coupling in van der Waals Ferromagnet Fe₃GeTe₂ Nanoflakes. *Phys. Rev. Lett.* **2020**, *125*, 047202.

(35) Hwang, I.; Coak, M. J.; Lee, N.; Ko, D. S.; Oh, Y.; Jeon, I.; Son, S.; Zhang, K.; Kim, J.; Park, J. G. Hard ferromagnetic van-der-Waals metal (Fe,Co)₃GeTe₂: a new platform for the study of low-dimensional magnetic quantum criticality. *J. Phys.: Condens. Matter* **2019**, *31*, 50LT01.

(36) Wang, X.; Li, Z.; Zhang, M.; Hou, T.; Zhao, J.; Li, L.; Rahman, A.; Xu, Z.; Gong, J.; Chi, Z.; Dai, R.; Wang, Z.; Qiao, Z.; Zhang, Z. Pressure-induced modification of the anomalous Hall effect in layered Fe₃GeTe₂. *Phys. Rev. B* **2019**, *100*, 014407.

(37) Wang, Y.; Wang, C.; Liang, S. J.; Ma, Z. C.; Xu, K.; Liu, X. W.; Zhang, L. L.; Admasu, A. S.; Cheong, S. W.; Wang, L. Z.; Chen, M. Y.; Liu, Z. L.; Cheng, B.; Ji, W.; Miao, F. Strain-Sensitive Magnetization Reversal of a van der Waals Magnet. *Adv. Mater.* **2020**, *32*, 7.

(38) Zhu, R.; Zhang, W.; Shen, W.; Wong, P. K. J.; Wang, Q.; Liang, Q.; Tian, Z.; Zhai, Y.; Qiu, C. W.; Wee, A. T. S. Exchange Bias in van der Waals CrCl₃/Fe₃GeTe₂ Heterostructures. *Nano Lett.* **2020**, *20*, 5030−5035.

(39) Kim, J.; Son, S.; Coak, M. J.; Hwang, I.; Lee, Y.; Zhang, K.; Park, J.-G. Observation of plateau-like magnetoresistance in twisted Fe₃GeTe₂/Fe₃GeTe₂ junction. *J. Appl. Phys.* **2020**, *128*, 093901.

(40) Hu, C.; Zhang, D.; Yan, F.; Li, Y.; Lv, Q.; Zhu, W.; Wei, Z.; Chang, K.; Wang, K. From two- to multi-state vertical spin valves without spacer layer based on Fe₃GeTe₂ van der Waals homo-junctions. *Sci. Bull.* **2020**, *65*, 1072−1077.

switching behavior in vdW-magnet/oxide heterostructure. *Adv. Mater.* **2025**, 2412037.

(41) Shan, J. Y.; Ye, M.; Chu, H.; Lee, S.; Park, J. G.; Balents, L.; Hsieh, D. Giant modulation of optical nonlinearity by Floquet engineering. *Nature* **2021**, *600*, 235−239.

(42) Xu, J.-M.; Wang, S.-Y.; Wang, W.-J.; Zhou, Y.-H.; Chen, X.-L.; Yang, Z.-R.; Qu, Z. Possible Tricritical Behavior and Anomalous Lattice Softening in van der Waals Itinerant Ferromagnet Fe$_3$GeTe$_2$ under High Pressure. *Chin. Phys. Lett.* **2020**, *37*, 076202.

(43) Huang, B.; McGuire, M. A.; May, A. F.; Xiao, D.; Jarillo-Herrero, P.; Xu, X. Emergent phenomena and proximity effects in two-dimensional magnets and heterostructures. *Nat. Mater.* **2020**, *19*, 1276−1289.

(44) Guo, J.; Zhou, Y.; Huang, C.; Cai, S.; Sheng, Y.; Gu, G.; Yang, C.; Lin, G.; Yang, K.; Li, A.; Wu, Q.; Xiang, T.; Sun, L. Crossover from two-dimensional to three-dimensional superconducting states in bismuth-based cuprate superconductor. *Nat. Phys.* **2020**, *16*, 295−300.

(45) Montanaro, A.; Giusti, F.; Zanfrognini, M.; Di Pietro, P.; Glerean, F.; Jarc, G.; Rigoni, E. M.; Mathengattil, S. Y.; Varsano, D.; Rontani, M.; Perucchi, A.; Molinari, E.; Fausti, D. Anomalous non-equilibrium response in black phosphorus to sub-gap mid-infrared excitation. *Nat. Commun.* **2022**, *13*, 2667.

(46) Ma, X.; Wang, Y.; Yin, Y.; Yue, B.; Dai, J.; Cheng, J.; Ji, J.; Jin, F.; Hong, F.; Wang, J. T.; et al. Dimensional Crossover Tuned by Pressure in Layered Magnetic NiPS$_3$. *Sci. China:Phys., Mech. Astron.* **2021**, *64*, 297011.

(47) Wang, Y.; Zhou, Z.; Wen, T.; Zhou, Y.; Li, N.; Han, F.; Xiao, Y.; Chow, P.; Sun, J.; Pravica, M.; Cornelius, A. L.; Yang, W.; Zhao, Y. Pressure-Driven Cooperative Spin-Crossover, Large-Volume Collapse, and Semiconductor-to-Metal Transition in Manganese(II) Honeycomb Lattices. *J. Am. Chem. Soc.* **2016**, *138*, 15751−15757.

(48) Zhang, H.; Niu, C.; Zhang, J.; Zou, L.; Zeng, Z.; Wang, X. Spin-crossover induced ferromagnetism and layer stacking-order change in pressurized 2D antiferromagnet MnPS$_3$. *Phys. Chem. Chem. Phys.* **2021**, *23*, 9679−9685.

(49) Harms, N. C.; Kim, H.-S.; Clune, A. J.; Smith, K. A.; O'Neal, K. R.; Haglund, A. V.; Mandrus, D. G.; Liu, Z.; Haule, K.; Vanderbilt, D.; Musfeldt, J. L. Piezochromism in the magnetic chalcogenide MnPS$_3$. *npj Quantum Mater.* **2020**, *5*, 56.

(50) Blochl, P. E. Projector augmented-wave method. *Phys. Rev. B* **1994**, *50*, 17953−17979.

(51) Kresse, G.; Furthmüller, J. Efficient iterative schemes for ab initio total-energy calculations using a plane-wave basis set. *Phys. Rev. B* **1996**, *54*, 11169.

(52) Grimme, S.; Antony, J.; Ehrlich, S.; Krieg, H. A consistent and accurate ab initio parametrization of density functional dispersion correction (DFT-D) for the 94 elements H-Pu. *J. Chem. Phys.* **2010**, *132*, 154104.

(53) Liu, N.; Wang, C.; Yan, C.; Xu, C.; Hu, J.; Zhang, Y.; Ji, W. Competing multiferroic phases in monolayer and few-layer NiI$_2$. *Phys. Rev. B* **2024**, *109*, 195422.

(54) Cococcioni, M.; De Gironcoli, S. Linear response approach to the calculation of the effective interaction parameters in the LDA+U method. *Phys. Rev. B* **2005**, *71*, 035105.

(55) Wu, Y.; Hu, Y.; Wang, C.; Zhou, X.; Hou, X.; Xia, W.; Zhang, Y.; Wang, J.; Ding, Y.; He, J.; Dong, P.; Bao, S.; Wen, J.; Guo, Y.; Watanabe, K.; Taniguchi, T.; Ji, W.; Wang, Z. J.; Li, J. Fe-Intercalation Dominated Ferromagnetism of van der Waals Fe$_3$GeTe$_2$. *Adv. Mater.* **2023**, *35*, 2302568.

(56) Ji, W.; Lu, Z.-Y.; Gao, H. Electron Core-Hole Interaction and Its Induced Ionic Structural Relaxation in Molecular Systems under X-Ray Irradiation. *Phys. Rev. Lett.* **2006**, *97*, 246101.

(57) Wang, C.; Qiao, J.; Pan, Y.; Zhou, L.; Kong, X.; Cheng, Z.; Chai, Y.; Ji, W. Charge tunable structural phase transitions in few-layer tellurium: a step toward building mono-elemental devices. *arXiv* **2018**, arXiv:1806.06550 preprint.